A Three-protein Charge Zipper Stabilizes a Complex Modulating Bacterial Gene Silencing*

Tiago N. Cordeiro[‡§1], **Jesús García**[¶], **Pau Bernadó**[§2], **Oscar Millet**[‖3], and **Miquel Pons**[‡4]

From the ‡Biomolecular NMR Laboratory, Department of Organic Chemistry, University of Barcelona, 08028 Barcelona, Spain, §Centre de Biochimie Structurale, INSERM U1054, CNRS UMR 5048, Université Montpellier 1 and 2, 34092 Montpellier, France, ¶Institute for Research in Biomedicine (IRB-Barcelona), 08028 Barcelona, Spain, and the ‖Structural Biology Unit, Center for Cooperative Research in Biosciences (CIC-bioGUNE), 48160 Elexalde, Derio, Spain

Background: The complex between Hha and H-NS selective represses genes in Enterobacteria acquired by horizontal transfer.
Results: A structural model for the regulatory complex is described.
Conclusion: A charge zipper formed by interdigitation of residues from three proteins stabilizes the complex.
Significance: Charge zippers provide selectivity to electrostatic protein complexes. Understanding selective gene silencing may help fighting antibiotic resistance.

The Hha/YmoA nucleoid-associated proteins help selectively silence horizontally acquired genetic material, including pathogenicity and antibiotic resistance genes and their maintenance in the absence of selective pressure. Members of the Hha family contribute to gene silencing by binding to the N-terminal dimerization domain of H-NS and modifying its selectivity. Hha-like proteins and the H-NS N-terminal domain are unusually rich in charged residues, and their interaction is mostly electrostatic-driven but, nonetheless, highly selective. The NMR-based structural model of the complex between Hha/YmoA and the H-NS N-terminal dimerization domain reveals that the origin of the selectivity is the formation of a three-protein charge zipper with interdigitated complementary charged residues from Hha and the two units of the H-NS dimer. The free form of YmoA shows collective microsecond-millisecond dynamics that can by measured by NMR relaxation dispersion experiments and shows a linear dependence with the salt concentration. The number of residues sensing the collective dynamics and the population of the minor form increased in the presence of H-NS. Additionally, a single residue mutation in YmoA (D43N) abolished H-NS binding and the dynamics of the apo-form, suggesting the dynamics and binding are functionally related.

The atomic coordinates and structure factors (code 2mw2) have been deposited in the Protein Data Bank (http://wwpdb.org/).
[1] Recipient of a fellowship from the Fundação Ciência e Tecnologia (Portugal).
[2] Supported by the CHEX SPIN-HD project of the Agence National de la Recherche and ATIP-Avenir.
[3] To whom correspondence may be addressed: Structural Biology Unit, Center for Cooperative Research in Biosciences (CIC-bioGUNE), Parque Científico Tecnológico de Bizkaia Bldg. 801A, 48160 Elexalde Derio, Spain. Tel.: 34-946572504; E-mail: omillet@cicbiogune.es.
[4] To whom correspondence may be addressed: Biomolecular NMR Laboratory, University of Barcelona, Cluster Building. Barcelona Science Park, Baldiri Reixac, 10-12 08028 Barcelona. Spain. Tel.: 34-934034683; E-mail: mpons@ub.edu.

Antibiotic resistance and the appearance of new virulent bacterial strains constitute a major threat to human health (1). The problem is aggravated by the transfer of resistance and virulence genes between bacteria (horizontal gene transfer) (2–4). In this context, a detailed knowledge of the mechanisms allowing bacteria to tolerate the acquisition of foreign DNA is lacking, and it may open the way to new sustainable strategies to fight infectious diseases. Proteins Hha and YmoA were first identified as environmental regulators of the expression of virulence factors in *Escherichia coli* (5) and *Yersinia* sp. (6), respectively. Hha/YmoA bind to the nucleoid-associated protein H-NS (7), enhance its capacity to silence newly acquired genes, and facilitate the smooth integration of foreign genes in the existing genome (8, 9). The key role of members of the Hha/YmoA family in enterobacteria is supported by their conservation in obligate endosymbionts (10) and their presence in conjugative plasmids (11). Hha is also directly involved in the formation and dispersal of biofilms, a microbial life-style that is responsible of many chronic infections and is associated with increased antibiotic tolerance and with resistance dissemination (12–14). Therefore, Hha/YmoA constitutes promising targets in the development of new antimicrobial drugs.

Hha and YmoA are homologous and functionally replaceable proteins (15, 16) with high sequence identity/homology (82.1/94.0%) and very similar structures formed by four helices separated by loops (17, 18). Interestingly, >30% of their primary structure corresponds to charged residues. The high degree of conservation (Fig. 1) and extensive mutational studies (19–21) suggest the relevant role of charged amino acids in Hha function. The N-terminal region of H-NS interacting with Hha is also unusually rich in charged residues (39%), reinforcing the notion that electrostatic interactions are essential for this interaction (19). The role of electrostatics is also supported by the ionic strength sensitivity of genes regulated through Hha·H-NS (22).

The putative role of electrostatic interactions in the Hha/YmoA complex with H-NS raises the problem of selectivity, as electrostatic interactions are often associated with nonspecific contacts in contrast to van der Waals interactions that display

high selectivity by means of an exquisite shape complementarity. The interaction of Hha/YmoA with H-NS is highly specific (19, 20).

In this article we have investigated the interplay between electrostatic forces and the constitutional and functional properties of Hha/YmoA. A detailed analysis of the structures of the Hha·H-NS complex in crystals (21) and in solution (first reported here) unraveled a charge zipper with conserved residues contributed by three proteins (Hha/YmoA and the two units of an antiparallel H-NS dimer). This feature explains the high selectivity of the Hha/YmoA interaction with H-NS. In addition, electrostatic repulsive interactions within YmoA are also responsible for the presence of collective slow motions (μs-ms) in the free form that, we argue, may also contribute to shape the biological function of Hha/YmoA.

Experimental Procedures

Protein Preparation—Unlabeled and isotopically enriched H-NS$_{46}$C21S (19), H-NS$_{64}$ (23), Hha variants (23), and YmoA variants (18) were expressed and purified as previously described. Single cysteine mutants were prepared by site-directed mutagenesis after substitution of the native cysteine by serine (H-NS) or isoleucine (Hha). Site-directed mutagenesis was carried using the QuikChange site-directed mutagenesis kit. All constructs were verified by DNA sequencing. Fluorescence anisotropy titrations were carried out to evaluate the affinity of YmoA toward H-NS$_{64}$ (24) at different ionic strengths.

NMR Samples for PRE[5] Experiments—Experimental intermolecular PRE data were obtained on samples containing ~100 μM ^{15}N-labeled H-NS$_{46}$C21S and 15–30 μM HhaC18I derivatized with MTSL at positions 37 or 66.

Additional experiments were carried out by observing ^{15}N-labeled HhaC18I in the presence of H-NS$_{46}$ dimer with an EDTA-Mn^{2+} tag placed in the C21 residue of each monomer. A third set of PRE experiments was carried out using ^{15}N-labeled H-NS$_{46}$C21S with an additional C-terminal cysteine tagged with 4-(2-iodoacetamide)-2,2,6,6-tetramethyl-1-piperidinyloxy radical (TEMPO). This sample was used to confirm the antiparallel topology of the H-NS$_{46}$ dimer. In all the PRE experiments the buffer was 20 mM HEPES (pH 7.0), 150 mM NaCl, and 0.01% (w/v) NaN$_3$. Adding a 2–3 molar excess of ascorbic acid generated diamagnetic reference samples of nitroxide radicals. EDTA-Ca^{2+}-tagged dimers were used as diamagnetic reference for the manganese-containing samples.

Spin Labeling—Derivatization reagents were 1-oxyl-2,2, 5,5-tetramethyl-3-pyrroline-3-methyl)-methanethiosulfonate (MTSL) or *N*-[S-(2-pyridythiol)cysteaminyl]-EDTA.

Proteins containing a single cysteine residue were incubated with 10 mM DTT at room temperature to ensure the reduction of any intermolecular disulfide bonds. The excess of DTT was removed by passing 2 times the reaction mixture through a

PD-10 column (GE Healthcare) (99.9% desalting capacity). After elution, protein solutions in 10 mM Tris (pH 7.4) (~100 μM) were mixed with a 10-fold molar excess of the derivatization reagent an incubated for 3 h in the dark at room temperature. To remove any unreacted tag, the resulting protein solution was passed 2× through a PD-10 column, and the buffer was exchanged to 20 mM HEPES (pH 7.0), 150 mM NaCl, and 0.01% (w/v) NaN$_3$. Complete incorporation of MTSL was confirmed by mass spectrometry, and the oligomeric state of the conjugated protein was checked by analytical gel filtration.

In the case of the cysteaminyl-EDTA adduct, the reaction was carried out in the presence of 1 mM MnCl$_2$ or CaCl$_2$ to generate the paramagnetic and diamagnetic samples. PRE measurements for the backbone amides were carried out at low molar fractions of complex (0.15–0.3) to reduce binding-induced broadening.

NMR Samples for CPMG Experiments—All ^{15}N-CPMG relaxation dispersion experiments were recorded on samples containing 1.1 mM YmoA protein (or variant) in 20 mM sodium phosphate, 1 mM (tris(2-carboxyethyl)phosphine), 0.2 mM EDTA, 0.01% (w/v) NaN$_3$, and 8% D$_2$O at pH 7.5 and 285 K and the stated concentration of NaCl and H-NS$_{64}$.

NMR Assignments—HhaC18I had been assigned previously (24). Assignments for the ^{1}H,^{15}N amide resonances of H-NS$_{46}$C21S were obtained using a combination of three-dimensional ^{1}H,^{15}N-edited NOESY-HSQC and ^{1}H,^{15}N-edited TOCSY-HSQC experiments acquired, with mixing times of 120 and 60 ms, respectively. Assignments have been deposited in Biological Magnetic Resonance Bank (25296).

YmoA backbone amide assignments were obtained based on published data (Biological Magnetic Resonance Bank entry 15486) (24) at pH 6.0 and 298 K. ^{1}H,^{15}N HSQC spectra of YmoA were stepwise recorded at pH 7.5, 7.0, 6.5, and 6.0 and then at 285, 292, and 298 K. Small ^{1}H,^{15}N chemical shift differences were observed for most residues and varied linearly with the temperature, such that the assignments at 298 K and pH 6.0 could be propagated to the other temperatures and pH values. ^{1}H,^{15}N HSQC NMR spectra of YmoA variants are similar to those of YmoA wild type and consistent with a well folded, monomeric protein with a similar overall structure.

PRE-guided Modeling—^{1}H,^{15}N HSQC spectra of diamagnetic and paramagnetic samples were acquired at 298 K with a recycling delay between scans of 2.5 s to ensure that magnetization recovery levels are identical for both states and using the same concentration and number of scans for both samples. NMR spectra were acquired on 600 MHz or 800 MHz Bruker spectrometers equipped with a TCI cryo-probe.

The paramagnetic contribution to the relaxation rate Γ_2 was determined using the ratio of peak intensities in the paramagnetic, and diamagnetic state (25),

$$\frac{I_{para}}{I_{dia}} = \frac{R_2^{dia} \exp(-\Gamma_2 t)}{R_2^{dia} + \Gamma_2} \qquad \text{(Eq. 1)}$$

where t is the evolution time during the INEPT transfer (set to ~10.63 ms; based on a ^{1}H,^{15}N scalar coupling of 94 H$_Z$); R_2^{dia} is transverse relaxation rate in the absence of paramagnets, which

---

[5] The abbreviations used are: PRE, paramagnetic relaxation enhancement; MTSL, 1-oxyl-2,2,5,5-tetramethyl-3-pyrroline-3-methyl)-methanethiosulfonate; TEMPO, 2,2,6,6-tetramethyl-1-piperidinyloxy; CPMG, Carr-Purcell-Meiboom-Gil; HSQC, heteronuclear single quantum correlation; AIR, ambiguous intermolecular distance restraint; T, tesla; SAXS, small-angle x-ray scattering; NTD, N-terminal dimerization domain; r.m.s.d., root mean square deviation.

TABLE 1
Interface restraints

Protein	Active residues	Passive residues
Hha	8, 25, 48	22, 29, 44, 45, 49, 52, 68
H-NS$_{46}$ [a]	9, 10, 12, 28	6, 11, 13, 15, 16, 31, 32, 35

[a] Residues of both chains were taken into account.

can be estimated for each residue from the line-width of the peak at half-maximum height.

Calculated PRE rates were converted into intermolecular distances using the equation,

$$d = \sqrt[6]{\frac{K}{\Gamma_{2,exp}^{DD}/p_b} \cdot \left(4 + \frac{3}{1 + \omega_H^2 \tau_c^2}\right)} \qquad \text{(Eq. 2)}$$

where K is 1.23×10^{-32} cm^6 s^{-2}, ω_H is the Larmor frequency of the proton, Γ_2 is the experimental determined PRE rate, p_b is the fraction of complex, τ_c is the correlation time estimated from Stokes-Einstein equation. The values of Γ_2 were corrected by $1/p_b$ to obtain the expected values for fully bound proteins. The correlation time for the electron-nuclear interaction was assumed to be equal to the global correlation time of the complex.

PRE effects from spin labels located at positions 37 and 66 were integrated as distance restraints together with mutagenesis data and chemical shift mapping (Fig. 3) in the HADDOCK docking approach (26). Interfacial residues were selected based in the fulfillment of at least three of the following criteria: (i) significant chemical shift perturbation upon the addition of small amounts of the interacting partner, (ii) at least 30% surface accessible area, (iii) as part of a cluster of residues that forms a plausible binding patch, (iv) mutation of the residue to give rise to a properly folded protein but with null or decreased binding ability. The selected residues were defined as "active" and their solvent accessible surface neighbors or residues that were in agreement with criteria (i) and (ii) as "passive." Haddock encodes these interfacial residues in terms of ambiguous intermolecular distance restraints (AIRs) to drive the docking (26). AIRs correspond to ambiguous distance between all atoms of the source residue (active) to all the atoms of all target residues (active and passive). The AIR definitions are provided in Table 1.

The known structures of free Hha (PDB 1JW2) and H-NS$_{46}$ dimer (PDB code 1NI8) were used as starting structures in the protein docking protocol. MTSL-modified cysteines were computational designed onto the surface of Hha starting structure. The mobility of the MTSL tags was taken into account by performing ensemble averaging of the PRE-driven restraints with four different MTSL orientations. All docking runs were performed using the HADDOCK standard docking protocol of three consecutive steps: (it0) rigid body energy minimization, (it1) semi-flexible refinement in the torsion angle space, and a final water refinement in explicit solvent (water). Hinges and flexible regions, paramagnetic tags, and/or residues identified as being part of the binding interface of a given model were considered explicitly as flexible in the it1- and water MD-simulated annealing refinement steps. The hinge prediction server HingeProt (27) was used to define the hinge regions of the flexible monomers. The number of structures was increased to

2000, 400, and 400 for it0, it1, and water, respectively. Random removal of AIRs was turned on. Other parameters were left to their default values. Scoring and clustering were performed according to standard HADDOCK procedures (28).

PRE effects on ^{15}N-HhaC18I caused by H-NS$_{46}$ with EDTA-Mn^{2+} placed in each Cys-21 residue were not used in the modeling and, therefore, provided an independent validation of the generated structures. Theoretical intermolecular PRE rates were back-calculated from the structural models using the Solomon-Bloembergen approximation by representing the paramagnetic label by an ensemble of states and calculating the order parameters accounting for the motion of the dipolar proton-electron interaction vector (29). The τ_c of each pose was estimated using HydroNMR (30). PRE rates were scaled by the population of the bound state and compared with the experimental values.

Side chain-directed HCACO Experiments—The standard HCACO experiment was modified to detect correlations between side-chain carbonyls and the adjacent β or γ methylene groups. In particular $C\beta/C\gamma$ excitation was achieved with a 320-μs Q5 pulse centered at 35 ppm. The experiments were run at 14.1 T and 298 K in a sample containing 0.7 mM ^{13}C-YmoA, 20 mM sodium phosphate buffer (pH 7.5) with 100 mM NaCl, 1 mM (tris(2-carboxyethyl)phosphine), 0.2 mM EDTA, and 0.01% (w/v) of NaN$_3$ in the absence or in the presence of 0.3 mM H-NS$_{64}$ to obtain about 40% of bound YmoA. We used a two-dimensional version of the experiment with 256 increments and 32 scans. Assignments were based on published data (Biological Magnetic Resonance Bank entry 15486).

CPMG Relaxation Dispersion Experiments—^{15}N-CPMG single-quantum relaxation dispersion experiments for YmoA were performed at 285K (calibrated with a methanol sample). Data sets were recorded always with two identical aliquots of the same freshly prepared protein sample on Bruker Avance III spectrometers operating at static magnetic fields of 14.1 and 18.8 T, the latter equipped with a cryo-probe.

All ^{15}N-CPMG relaxation dispersions were collected as a series of two-dimensional planes with 16 interleaved frequency ν_{cp} values, ranging from 25 to 1000 Hz, including 2 repeats for error analysis and using a constant-time version (31) of the relaxation-compensated TROSY CPMG pulse scheme (32). Each two-dimensional spectrum was recorded with 180 and 200 complex points in t_1 dimension at 14.1 T and 18.8 T, respectively, and a delay between scans of 1.2 s. The total constant-time-CPMG relaxation T_{relax} delay was set to 80 ms. A compensation element was applied at the beginning of each scan to suppress artifacts due to ν_{cp}-dependent changes in sample temperature.

Effective relaxation rates, $R_{2,eff}$, were calculated according to the relation (33),

$$R_{2,eff}(\nu_{cp}) = -\frac{1}{T_{relax}} \ln\left(\frac{I(\nu_{cp})}{I_0}\right) \qquad \text{(Eq. 3)}$$

where I_0 is the intensity of a peak in the reference spectrum recorded without CPMG relaxation delay, and $I(\nu_{cp})$ is the corresponding peak intensity in the spectrum measured at a frequency of ν_{cp}.

Dispersion profiles for each ^{15}N were individually and globally analyzed to obtain values of $k_{ex} = k_+ + k_-$ by fitting the Carver-Richards equation (34) using in-house Matlab scripts either to one field alone or simultaneously using data from two fields.

Electrostatic Potentials and Clustering—We used Poisson-Boltzmann electrostatic calculations and homology modeling to quantitatively identify regions of conserved electrostatic character (35, 36) in the Hha/YmoA family of proteins. Homology modeling was used to generate structures for the Hha homologues with unsolved structures based on PDB code 1JW2 using SWISS-MODEL (37). All protein sequences were taken for UniProt (38).

All electrostatic potential calculations were performed using DelPhi (39) with $129 \times 129 \times 129$ grid points, considering solvent dielectric constant of 80 with an ion concentration of 200 mM, whereas the protein dielectric constant was 4. A probe with a radius of 1.4 Å was used to define the dielectric boundary. Each electrostatic potential calculation was centered on each structure to ensure proper alignment of electrostatic potentials before similarity calculations.

Similarity matrices were generated based on the electrostatic similarity index as defined elsewhere (35, 36). Cumulative distributions of electrostatic conservation index (ECI) were calculated using (40),

$$ECI = \frac{1}{N} \sum_{i \times 1}^{N} - \frac{|\varphi_A| - |\varphi_{B,i}|}{\max(|\varphi_A|, |\varphi_{B,i}|)} \qquad \text{(Eq. 4)}$$

Here φ_A represents the electrostatic potential of *E. coli* Hha to which all other potentials $\varphi_{B,i}$ were compared. The electrostatic conservation index is calculated at each grid point and normalized by N, the number of electrostatic potentials comparisons, which are in total 12. The electrostatic conservation only describes the similarity of the electrostatic potential of a set of proteins to one particular protein at a given grid point. The surface projections of electrostatic conservation were generated using UCSF Chimera (41).

Small-angle X-ray Scattering (SAXS) Experiments—SAXS data were measured in the beam-line BM29 (ESRF-Grenoble). Data were collected at multiple concentrations from 0.9 to 10 mg/ml at 285 K in 20 mM phosphate buffer (pH 7.5), 100 mM NaCl, 1 mM (tris(2-carboxyethyl)phosphine), 0.2 mM EDTA and 0.01% NaN$_3$. A momentum transfer range of 0.032–4.93 Å^{-1} was measured. Repetitive measurements indicated that samples did not present radiation damage.

Because the relative populations of species in solution change as a function of the concentration, the final SAXS profiles were directly used without merging them. Initial points of the curves were discarded for the analysis to minimize interparticle interaction effects. Data processing was performed using PRIMUS (42). The theoretical SAXS curves of full-length YmoA, H-N$_{64}$, and YmoA·H-NS$_{64}$ complexes were computed using the program CRYSOL (43). All theoretical curves were computed with 101 points and a maximum scattering vector of 0.5. Flexibility was accounted for by averaging ensembles of ~1000 structures. Theoretical curves for YmoA·H-NS$_{64}$ mix-

tures were computed by linear combination of the theoretical curves of the individual species weighted by their predicted population in the mixture. The binding constant was obtained from fluorescence anisotropy titrations. Experimental and predicted curves were directly compared with no adjustable parameter fitting.

Results

Electrostatics in the Hha/YmoA Family of Proteins—To investigate the role of electrostatic forces in the function of Hha-like proteins, we first examined the conservation of the charge distribution across this family of proteins. For this purpose we chose 13 Hha homologues differing in sequence (37.1–98.6% identity with *E. coli* Hha) and net charge (-0.8 to $+6$) and computed their electrostatic potentials using structural templates generated by homology modeling from the Hha structure (PDB code 1JW2). The isopotential surfaces shown in Fig. 1*B* clearly show a similar asymmetrical electrostatic potential distribution. Quantitative pairwise electrostatic similarity calculations (35) show that chromosomic Hha paralogues cluster together, whereas Hha-like proteins from plasmids and the obligate endosymbiont *Wigglesworthia glossinidia* form a separate cluster (Fig. 1*C*). Fig. 1*D* shows the local degree of conservation of the electrostatic potential between the 13 homologues, mapped on the Hha structure compared with the conservation in the amino acid sequence. Thus, the abundance of charged residues and their distribution seems to be a conserved feature of members of the Hha/YmoA family, suggesting a functional role.

Solution Structure of the Hha·H-NS$_{46}$ Complex; a Three-protein Charge Zipper—To unravel the role of electrostatics in the molecular recognition associated to Hha, we determined the solution structure of Hha bound to H-NS. H-NS contains an oligomerization and a DNA binding domain separated by a linker. Two dimerization regions connected by a long α-helix form the oligomerization domain (44). Hha interacts exclusively with the N-terminal dimerization domain (NTD) of H-NS. The NTD is completely included in a construct formed by residues 2–47 (H-NS$_{46}$) (19, 45). The solution structure of the complex formed between Hha and H-NS$_{46}$ could not be determined by classical NOE-based methods because of extensive broadening of key NMR signals upon complex formation. Therefore, we turned to PRE NMR experiments as a source of structural restraints (46). This approach allows the observation of residues distant from the paramagnetic tag, even at low molar fractions of complex where intrinsic broadening associated to complex formation is minimized. Paramagnetic tags were introduced by reaction MTSL in four single cysteine variants of Hha: wild type Hha (C18) and three single cysteine mutants at positions 37, 66, and a non-native C-terminal position 74. In these mutants cysteine 18 was mutated to isoleucine. The C18I mutation had been previously shown not to affect H-NS binding (24). Paramagnetic effects were measured on ^{15}N-labeled H-NS$_{46}$ C21S. The native cysteine in H-NS$_{46}$ (Cys-21) was mutated to serine to avoid MTSL exchange. The labeled positions (Fig. 2*A*) are located outside of the H-NS binding interface inferred by perturbations mapping (Fig. 3). The addition of Hha spin-labeled at positions 37 and 66 to ^{15}N-labeled

Structure of the H-NS Hha Charge Zipper Complex
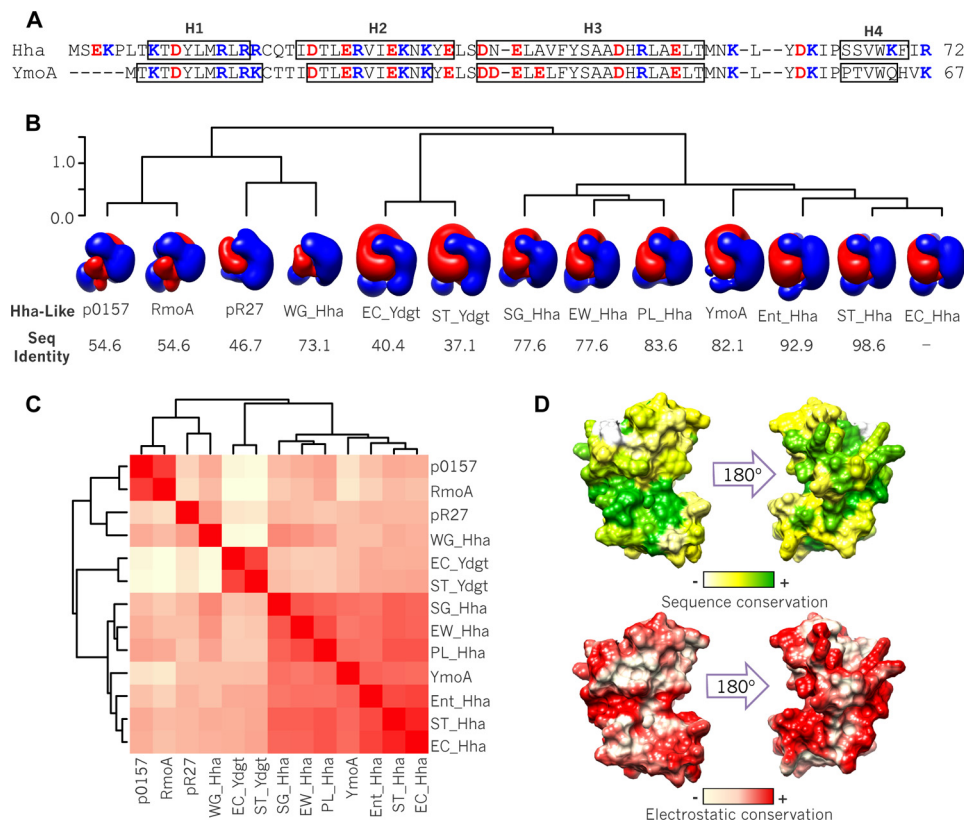
FIGURE 1. **Electrostatics conservation in Hha/YmoA family.** *A*, sequence and secondary structure of Hha/YmoA. *Open boxes* denote α-helical regions. *B*, clustering of 13 Hha-like proteins according to the similarity of their electrostatic potential: EC-Hha (*E. coli* Hha), ST-Hha (*Salmonella enterica* serovar Typhimurium Hha), Ent-Hha (*Enterobacter cloacae* Hha), YmoA (*Yersinia* spp. YmoA), PL-Hha (*Photorhabdus luminescens* Hha), EW-Hha (*Erwinia carotovora* Hha), WG-Hha (*W. glossinidia* Hha), SG-Hha (*Sodalis glossinidius* Hha), Rmoa (plasmid R100 RmoA), p0157 (plasmid p0157 Hha), pR27 (plasmid R27 Hha), EC-YdgT (*E. coli* YdgT), and ST-YdgT (*S. enterica* serovar Typhimurium YdgT). Negative (*red*) and positive (*blue*) isopotential contours of each protein are represented. The percentage of sequence identity with respect to EC-Hha is shown below. *C*, heat-map showing the pairwise electrostatic similarities. The scale is relative from low (*light yellow*) to high (*red*) ES. *D*, the local conservation of sequence (*top*) and electrostatic potential (*bottom*) of the ensemble of 13 proteins with respect to *E. coli* Hha is mapped on the surface of Hha.

H-NS$_{46}$ C21S resulted in selective intermolecular PRE distance-dependent broadening of H-NS$_{46}$ ^{1}H,^{15}N resonances (Fig. 2*B*), whereas no effect was observed when MTSL was attached at positions 18 or 74 of Hha. PRE data, binding-induced broadening, and mutagenesis information were converted into structural restraints and used in a flexible Haddock docking protocol starting with the known structures of unbound Hha (PDB code 1JW2) (17) and H-NS$_{46}$ antiparallel dimer (PDB code 1NI8) (47). The solution structures were validated with an additional set of independent PREs. The structural models correctly predicted the intermolecular PRE obtained by incorporating a paramagnetic tag, EDTA-Mn^{2+}, in each Cys-21 residue of H-NS$_{46}$ dimer (Fig. 2*C*) and measuring the paramagnetic effects on ^{15}N-labeled Hha (Fig. 2*D*).

Structural statistics are given in Table 2. An ensemble of structures derived from PRE-driven modeling has been deposited in the PDB (PDB code 2mw2, RCSB number RSCB104115, Biological Magnetic Resonance Bank accession code 25296). The most relevant feature shared by all the models in the ensemble is the presence of an interdigitated array of residues with alternating charges, forming an electrostatic zipper (Fig. 4). The involved residues belong to three molecules, Hha and the two molecules (A and B) that constitute the H-NS$_{46}$ dimer: Glu-25 (Hha)-Arg-12 (H-NS$_{46}$-A)-Asp-48 (Hha)-Lys-32 (H-NS$_{46}$-B). Fig. 3*B* shows a close-up view of the electrostatic zip-

per in the Hha·H-NS model structure. Although the electrostatic interactions in the charge zipper probably dominate, additional contacts that also contribute to the complex stability are shown in Fig. 5.

The charge zipper model explains the known effect of mutations in Hha (D48E and E25Q) and H-NS (R12K) (19, 20). It also predicted that Lys-32 of H-NS should be essential for the interaction. Indeed, this prediction was experimentally confirmed: mutation to glutamine of Lys-32 in H-NS leads to the complete loss of Hha binding (Fig. 6). The K32Q mutant and the wild type form have nearly identical circular dichroism spectra, confirming that the mutation does not affect the folding of H-NS (data not shown). Similar effects were observed in YmoA and YdgT (20), suggesting that H-NS complexes formed by other members of the Hha/YmoA family involve a similar charge zipper.

We confirmed the participation of aspartic and glutamic acid side chains of YmoA in its complex with H-NS$_{64}$, a truncated H-NS construct comprising residues 1–64, using a HCACO experiment modified to detect the correlation between side-chain carbonyl groups and their adjacent methylene groups (Fig. 6*C*). The experiments were done with ^{13}C-labeled YmoA because, in comparison with Hha, it has one more acidic group predicted to participate in the charge zipper (Asp-43, Glu-36, Glu-20 in YmoA; Asp-48, Ala-41, Glu-25 in Hha).
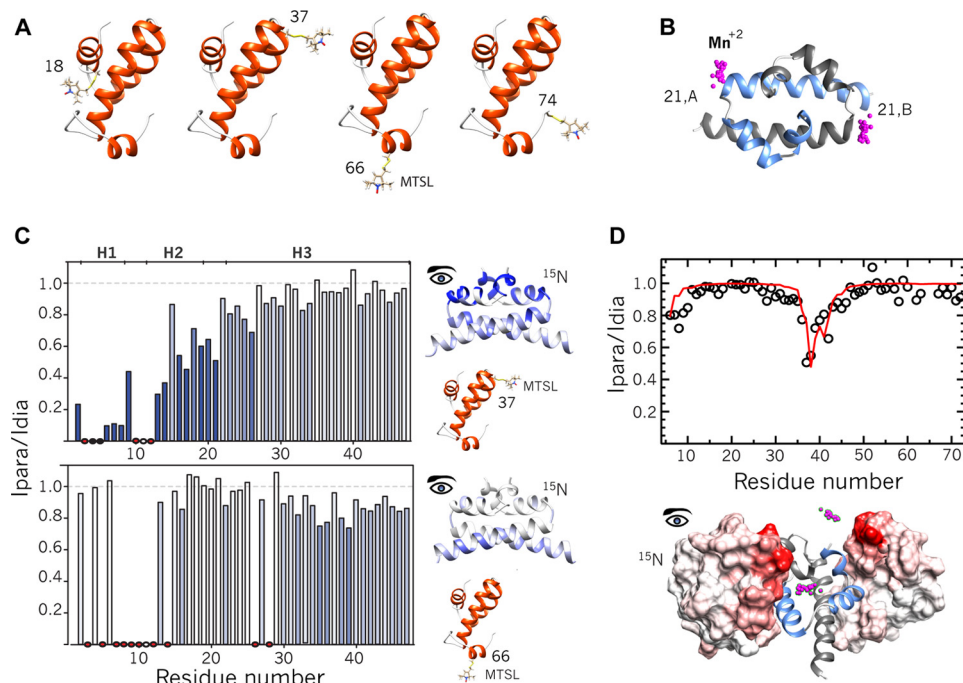
FIGURE 2. **Paramagnetic relaxation enhancement experiments.** *A*, MTSL-tagging of singled-cysteine Hha variants. Nitroxide spin labels located at different points in Hha structure are rendered in sticks. *B*, EDTA-Mn^{2+} tagging positions on H-NS$_{46}$ dimer. Mn^{2+} (paramagnetic centers) atoms are displayed as *magenta spheres*, representing the flexibility of the tag. *C*, intermolecular PRE restraints. The histograms show the experimental intensity ratios of each amide resonance of ^{15}N-H-NS$_{46}$C21S in the presence of substoichiometric amounts of Hha at natural isotopic abundance, with MTSL conjugated at D37C or S66C. *Ipara* is the intensity in the paramagnetic sample, and *Idia* is the intensity in the corresponding diamagnetic control. Signals that disappear in paramagnetic conditions are indicated by *black dots*. *Red dots* identify residues that could not be accurately measured due to broadening caused by complexation. *White circles* indicate missing signals. Stronger intermolecular PREs are displayed on H-NS$_{46}$ structure and highlighted on the PRE profiles in *blue scale*. PRE ratios were converted into intermolecular distance restraints. *D*, intermolecular paramagnetic effects (*open circles*) induced on the backbone amide resonance of ^{15}N-HhaC18I by EDTA-Mn^{2+} attached to H-NS$_{46}$ The *solid red line* represents the average PRE profile predicted from the best structures. The *inset* displays the PREs effects mapped on the surface of representative Hha structures of both clusters.
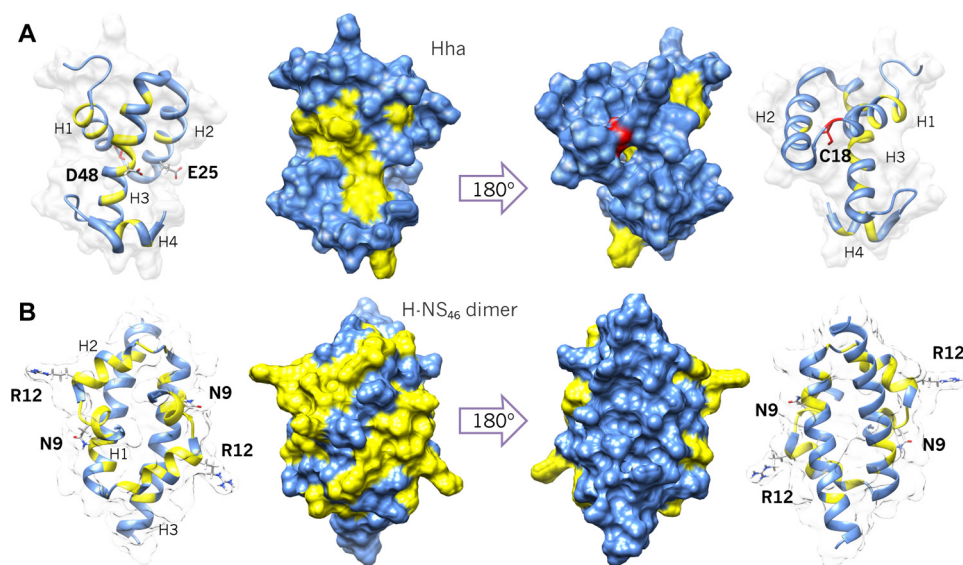
FIGURE 3. **Hha·H-NS interaction mapping.** *A*, Hha residues most affected by broadening in the presence of 0.5 eq of H-NS$_{64}$ are highlighted in *yellow* on ribbon and surface representations of Hha structure. C18 (in *red*) mutants do not affect H-NS binding. Asp-48 and Glu-25 mutants show null or reduced affinity toward H-NS. These residues are located in the same side of Hha structure, whereas C18 is located on the opposite side of H-NS binding site. *B*, H-NS$_{46}$ residues most affected by the addition of Hha are highlighted in *yellow*. The Hha binding region is located around the first two helices of H-NS and R12 is essential for Hha binding. N9 mutants also strongly reduce Hha binding.

As predicted by the charge zipper model, the addition of H-NS$_{64}$ results in large changes in Asp-43 and Glu-36. Glu-20 is in a crowded region. Residue Glu-29, located in a loop and not predicted to interact directly or indirectly with H-NS, is not affected by the addition of H-NS$_{64}$ and acts as a negative control. Residue Asp-56 is also located in a loop, but it forms an intramolecular salt bridge that contributes to positioning of helix 4 that is in contact with H-NS in the complex. Therefore, the intramolecular salt bridge is indirectly perturbed by the addition of H-NS$_{64}$ and Asp-56 provides a positive control.

Structure of the H-NS Hha Charge Zipper Complex

TABLE 2
Structural statistics

	Cluster 1
Interface restraints	
PRE restraints	31
AIRS[a]	7
Structure statistics	
Violations	
AIR deviations	1.36 ± 0.48
PRE deviations	1.51 ± 0.54
Deviations from idealized geometry	
Bond lengths (Å)	0.0030 ± 0.0001
Bond angles (°)	0.65 ± 0.05
Average pairwise r.m.s.d.[b] (Å)	
Backbone	0.85 ± 0.13
All atoms	1.41 ± 0.10
Ramachandran analysis[b]	
Most favored regions	95.99 ± 1.57%
Additional allowed regions	2.23 ± 1.46%
Generously allowed regions	0.84 ± 0.55%
Disallowed regions	0.98 ± 0.36%

[a] See Table 1.
[b] Ramachandran analysis was performed using PROCHECK.
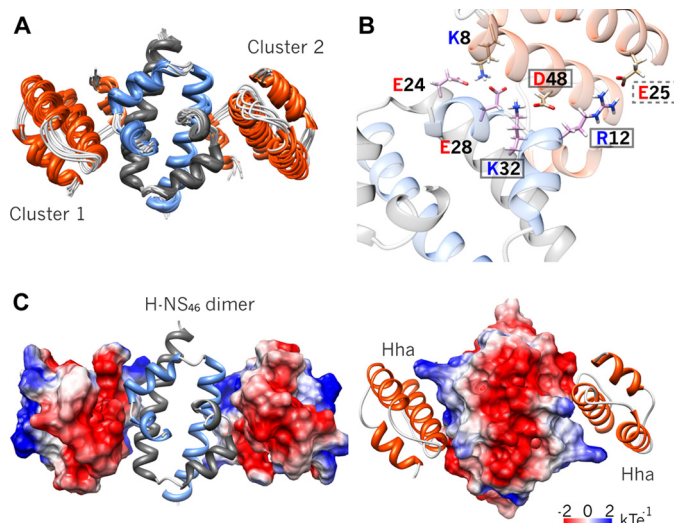
FIGURE 4. **Hha·H-NS charge zipper.** *A*, superposition of the 10 lowest energy PRE-derived solution complex structures. Hha (*orange*) and H-NS$_{46}$ dimer (*light blue* and *gray*) are shown in ribbon representations. All models satisfy the experimental data clustered into two equivalent solutions. *B*, close-up of the charge zipper interface. The *solid* and *dashed-line boxes* denote residues, whose mutation completely or nearly abolishes the binding, respectively. *C*, surface representations of the electrostatics potential of Hha and H-NS$_{46}$ show that the complex is stabilized by charge complementary.

Our solution structural model of the Hha·H-NS complex can be compared with the recently published crystal structure of an equivalent complex (21). Despite the fact that the crystal structure has missing electron density for atoms in 50 side chains, including most of the interface region, the x-ray and NMR models have very similar backbone structures. The closest structures have a root-mean-square difference (r.m.s.d.) of ~1.6 Å, confirming the overall geometry of the complex. Modeling the missing side chains in the x-ray structure also leads to a charge zipper (results not shown).

Fig. 7 shows a comparison of the NMR and x-ray models. The x-ray structure was obtained with an excess of Hha to saturate the two binding sites in the H-NS dimer. Based on the measured binding constant, the population of the species with two Hha molecules bound to the H-NS dimer should be very low under our experimental NMR conditions.

The structure of the YmoA·H-NS$_{64}$ complex was predicted by homology based on the Hha·H-NS structure (Fig. 6D). SAXS of YmoA in the presence of H-NS$_{64}$ was in good agreement with predictions based on the structures of YmoA, H-NS$_{64}$, and models of the YmoA·H-NS$_{64}$ complexes (one or two YmoA molecules per H-NS dimers) weighted according to the populations predicted by the experimental binding constant, assumed to be identical for the two sites in the H-NS dimer (Fig. 8). These results confirm the structure of the Hha·H-NS complex, the independent binding to the two sites, and the similarity between the complexes formed by Hha and YmoA.

The two bound Hha molecules in the crystal structure are not equivalent by symmetry. Although all the PRE-based models present the charge zipper, they also fall into two structural clusters. One of the x-ray determined sites is similar to one of the clusters, but it has a r.m.s.d. higher than 2.7 Å to the members of the second cluster. The second x-ray model shows intermediate r.m.s.d. values to the PRE-based models. The major difference between the various models and the structure of free Hha involves changes in the position of helix 4 that is displaced to allow H-NS binding and conformational changes in residues spatially close to Asp-48 (Tyr-44 and Trp-68) to allow key residues to interact with H-NS. The observed structural variability, the missing electronic density within the crystallographic Hha·H-NS interface, and previous NMR data (23) suggest the existence of dynamics in the Hha protein family.

YmoA Shows Concerted Pervasive Microsecond-Millisecond Dynamics—Dynamics of free YmoA was studied using CPMG relaxation dispersion measurements for the backbone amide group and at two magnetic fields (14.1 and 18.8 T). Hha samples tend to aggregate at the concentrations required for these experiments, whereas the YmoA construct used by McFeeters *et al.* (18) is highly soluble and stable over long periods at 1.1 mM in 20 mM sodium phosphate, 200 mM NaCl, pH 7.5 and 285 K.

Fig. 9 shows representative dispersion curves. CPMG relaxation dispersion curves were analyzed as an equilibrium between two sites characterized by resonance frequencies ω_A and ω_B with populations p_A and p_B, respectively, exchanging at a rate $k_{ex} = k_+ + k_-$ (34). A preliminary analysis of the relaxation dispersion curves of individual residues showed dynamics in 12 residues with similar apparent k_{ex} values distributed along the entire sequence: Leu-7 in helix1, Glu-24 and Lys-27 in helix 2, Asp-33, Tyr-39, Ala-42, and Asp-43 in helix 3, Tyr-55 and Ile-58 in a loop, and Val-62, Gln-64, and His-65 in the C-terminal helical region. The spatial distribution of the dynamic residues and the similar k_{ex} values found for the exchanging residues suggest concerted dynamics affecting large regions or the entire protein. Therefore, the dispersion curves were analyzed collectively assuming that groups of residues move in a concerted way (*i.e.* with the same k_{ex} and p_B). A protocol for residue incorporation, based on F-test analysis, was created. Two groups were identified, a first group including residues 55, 58, 64, and 65 that can be fitted collectively with a $k_{ex} = 267 ± 85$ s^{-1} and $p_B = 6 ± 2\%$. These residues are located in helix 4 and the loop that connects it to helix 3, a region showing major structural differences among the different existing structures of the Hha/YmoA family.
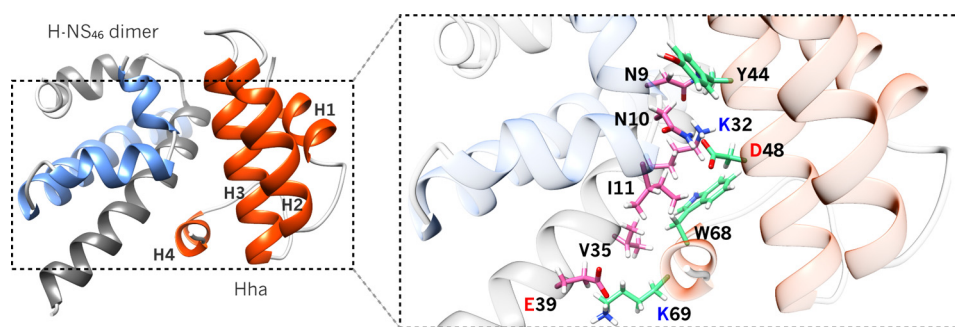
FIGURE 5. **Additional hydrophobic contacts in Hha·H-NS₄₆ complex.** Ribbon representation of the atomic model obtained by combining PRE, chemical shift perturbations, and mutagenesis data showing Hha in *orange* and H-NS₄₆ dimer in *gray/blue*. Residues at the interface are shown in *pink* (H-NS₄₆) or *green* (Hha) sticks. In addition to electrostatics complementary (Fig. 3), the complex is also stabilized by hydrophobic contacts, flanking the salt bridge formed by Asp-48 (Hha) and Lys-32 (H-NS₄₆).
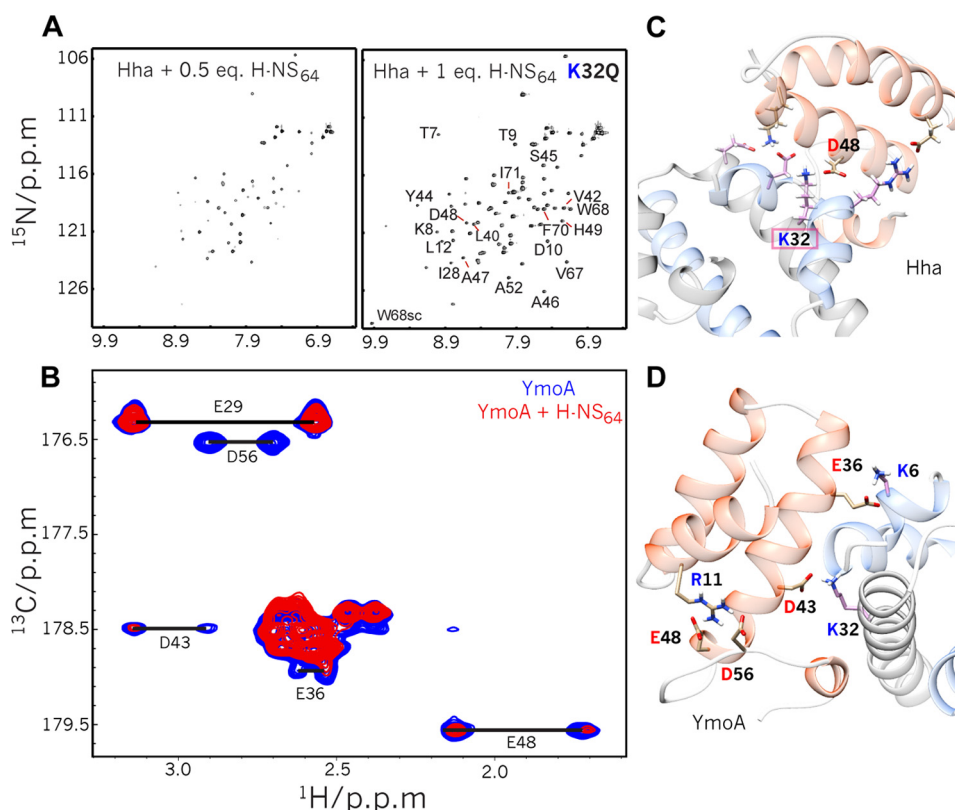
FIGURE 6. **Corroborating experimental evidence for the charge zipper.** *A*, ^{1}H,^{15}N HSQC spectra of ^{15}N-labeled Hha in the presence of 0.5 eq of wild-type H-NS₆₄ (*left panel*) or 1 eq of H-NS₆₄ K32Q mutant (*right panel*). Residues showing >75% reduction in their intensities upon the addition of H-NS₆₄ are indicated. The spectra of YmoA free and in the presence of NS₆₄ K32Q are identical, indicating that the K32Q mutation completely prevents the interaction. *B*, modified HCACO spectra of ^{13}C-YmoA showing the correlation between side-chain carbonyls of Asp and Glu residues and the corresponding β and γ protons in the absence (*blue*) and in the presence of H-NS₆₄. *C*, close-up view of the structure of the Hha·H-NS complex. The residue Lys-32 is located in the center of the charge zipper at the complex interface, forming a salt bridge with Asp-48 of Hha. *D*, close-up view of the structure of the YmoA·H-NS complex generated by homology modeling from the Hha·H-NS complex. YmoA side chains that are perturbed in the presence of H-NS₆₄ (*panel B*) are indicated.

A second group of dynamic residues (24, 27, 39, 42, and 43) is located in helices 2 and 3, constituting the structural core region of the Hha/YmoA family, well conserved in Hha, YmoA, and YdgT. These residues could be collectively fitted using $k_{ex} = 1200 \pm 130$ s^{-1} and $p_B = 2 \pm 1\%$. Under the assumption of the two-state model, the derived kinetic constants for the process are: $k_+ = 1177 \pm 65$ s^{-1} and $k_- = 23 \pm 8$ s^{-1}.

Residues that could not be incorporated in any of the two groups were further analyzed using a three-state model based on the simultaneous occurrence of the two previously defined processes. A good fit was obtained, but an F-test analysis

showed that the improvement with respect to an independent two-state model was not significant.

The existence of concerted dynamics raises the question of the functional coupling between YmoA dynamics and H-NS binding. To address this question, we measured CPMG relaxation dispersion of YmoA in the presence of increasing amounts (40 and 80 μM resulting in 3 and 6% bound YmoA, respectively) of H-NS₆₄. The low concentrations of H-NS₆₄ had little effect in the observed spectra but significantly affected the dynamics observed in the CPMG experiment. In the presence of 40 (80) μM H-NS₆₄ the number of residues showing millisec-
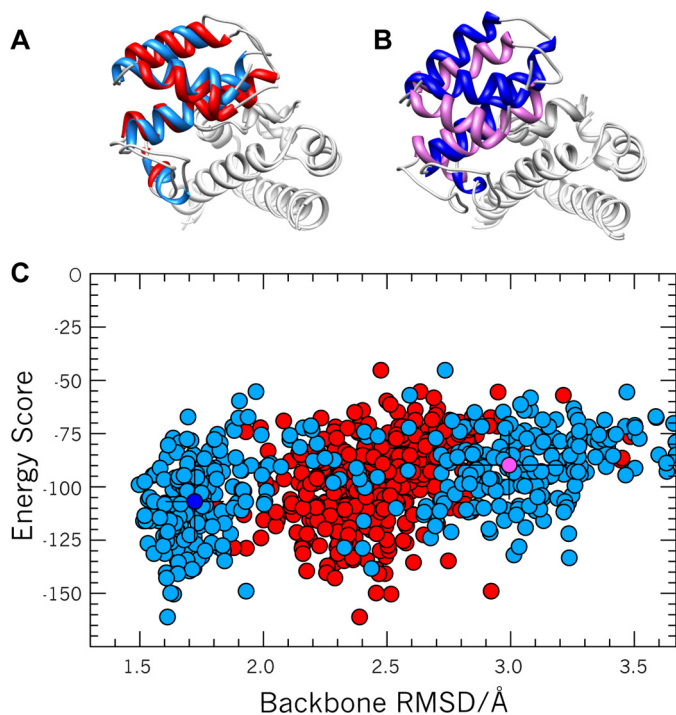
FIGURE 7. **Comparison of x-ray and solution models of Hha·(H-NS$_{46}$)$_2$ complexes.** *A*, superimposition of the two Hha molecules in the x-ray structure of Ali *et al.* (21) using the H-NS$_{46}$ molecules with which they interact as a reference. Hha molecules are shown in *red* and *light blue*. *B*, comparison of the location of Hha in representative structures of both clusters shown in *blue* and *pink ribbon* representations. *C*, r.m.s.d. of the 400 best Hha models derived from solution experiments to the two Hha models derived from x-ray diffraction. The color code is the same. Using the x-ray model depicted in *light blue* as a reference, the solution models fall into two clusters with low (1.73 ± 0.12 Å) and high (2.99 ± 0.23 Å) r.m.s.d. In contrast, using the "red" x-ray model, the solution models fall in a single cluster with intermediate r.m.s.d. (1.9–2.7 Å).

ond dynamics increased from 12 to 21 (38) residues of YmoA. Although H-NS$_{64}$ binding in the presence of intrinsic dynamics in the apo form would in principle call for at least a three-state model, an F-test analysis showed that the improvement of the fit was not statistically significant with respect to the two-state model. The small concentration of complex present thus appears as a perturbation of the apoprotein dynamics, and data measured in the presence of H-NS were analyzed with a two-state model with concerted dynamics, as in the free YmoA but incorporating additional residues to the group in the core region that participate in the concerted dynamics. The similarity of the structures of the core regions of free and bound forms in the case of Hha support the idea that H-NS binding affects mostly the dynamics of YmoA.

Residues in helix 4 showed a complex response to the addition of H-NS. The structural variability in the position of helix 4 in free YmoA is probably aggravated by the formation of the complex with H-NS. The effect of H-NS$_{64}$ addition on the side chain of a key residue in the loop that connects helices 3 and 4 supports the idea of more complex structural changes in this region, although a three-state model did not improve the fit with respect to the two-state one, and no further analysis was attempted.

The population of the minor species sensed by the core residues increased from 2% in the free form to 5–6% in the presence of 6% H-NS-bound species (Table 3). Remarkably, these
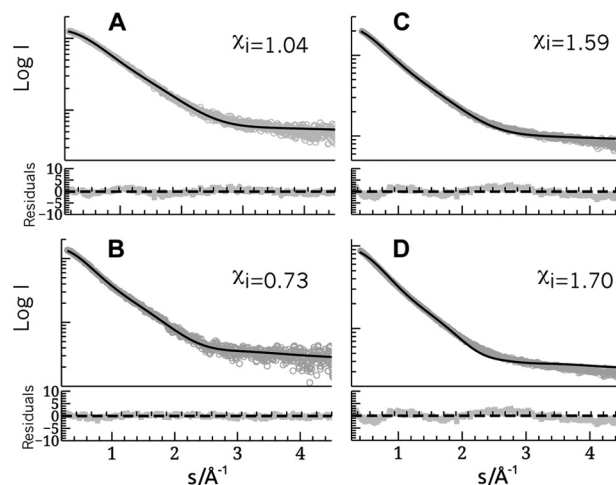
FIGURE 8. **SAXS data confirm the homology models of YmoA·H-NS$_{64}$ complexes.** Comparison of experimental (*circles*) and calculated (*continuous lines*) SAXS curves. *A*, pure YmoA. The theoretical curve was based on the NMR structure (18) allowing for flexibility in the connection between helices 3 and 4. *B*, pure H-NS$_{64}$. The theoretical curve of the H-NS$_{64}$ dimer was extracted from the x-ray structure of an H-NS oligomer and adding the flexible His tag. *C* and *D*, YmoA and HNS$_{64}$ mixtures. The YmoA·H-NS$_{64}$ complexes were modeled using the Hha·H-NS structure presented in this study and allowing the same level of flexibility that the free partners. The molar fractions of the species, calculated on the basis of the binding constant and the actual concentrations, were 0.73 (YmoA), 0.03 (H-NS$_{64}$ dimer), 0.12 H-NS$_{64}$-YmoA (2:1), and 0.12 (H-NS$_{64}$-YmoA (2:2) (*C*) and 0.46 (YmoA), 0.10 (H-NS$_{64}$ dimer), (0.26 (H-NS$_{64}$-YmoA (2:1)), and 0.16 (H-NS$_{64}$-YmoA (2:2)) (*D*). The quality of the agreement can be evaluated from the residuals shown *below each curve* and their individual figure of merit χi).

populations agree, within experimental error, with the complex concentrations derived from the association constant. Finally, although the apparent k_{ex} value remained largely unaltered within experimental error (1200 ± 130 s^{-1} (free), 1162 ± 104 s^{-1} (40 μM H-NS$_{64}$), 1240 ± 116 s^{-1} (80 μM H-NS$_{64}$)), the resulting kinetic constants showed a constant increase in k_-, whereas k_+ remained constant within experimental error (Table 3). The simplest model explaining the experimental observations is that binding of H-NS is coupled with the intrinsic dynamics of YmoA, which may also have an electrostatic origin.

Ionic Strength Effects and Mutagenesis Show That YmoA Dynamics and H-NS Binding Are Related—Because of the electrostatic character of the YmoA·H-NS interface, we characterized the stability of the complex as a function of ionic strength (200 mM, 100 mM, and 50 mM NaCl). The dissociation constants (K_D) for the YmoA·H-NS$_{46}$ complex increases linearly with the salt concentration (Fig. 9), suggesting that electrostatic effects are important for complex formation but through their effect on the off-rate, as an effect of the ionic strength in the on-rate should result in strong deviations from linearity (48).

The increase in stability of the complex at low ionic strength is consistent with the charge zipper motif identified in the NMR structure of the Hha·H-NS complex. The high charge density in free YmoA, when not compensated by the interaction with H-NS, is expected to create intramolecular electrostatic interactions, which may be the origin for the dynamics observed in YmoA. To test this hypothesis we compared CPMG relaxation dispersion experiments of free YmoA at 200 mM, 100 mM, and 50 mM NaCl (Fig. 10 and Table 3). When the salt concentration
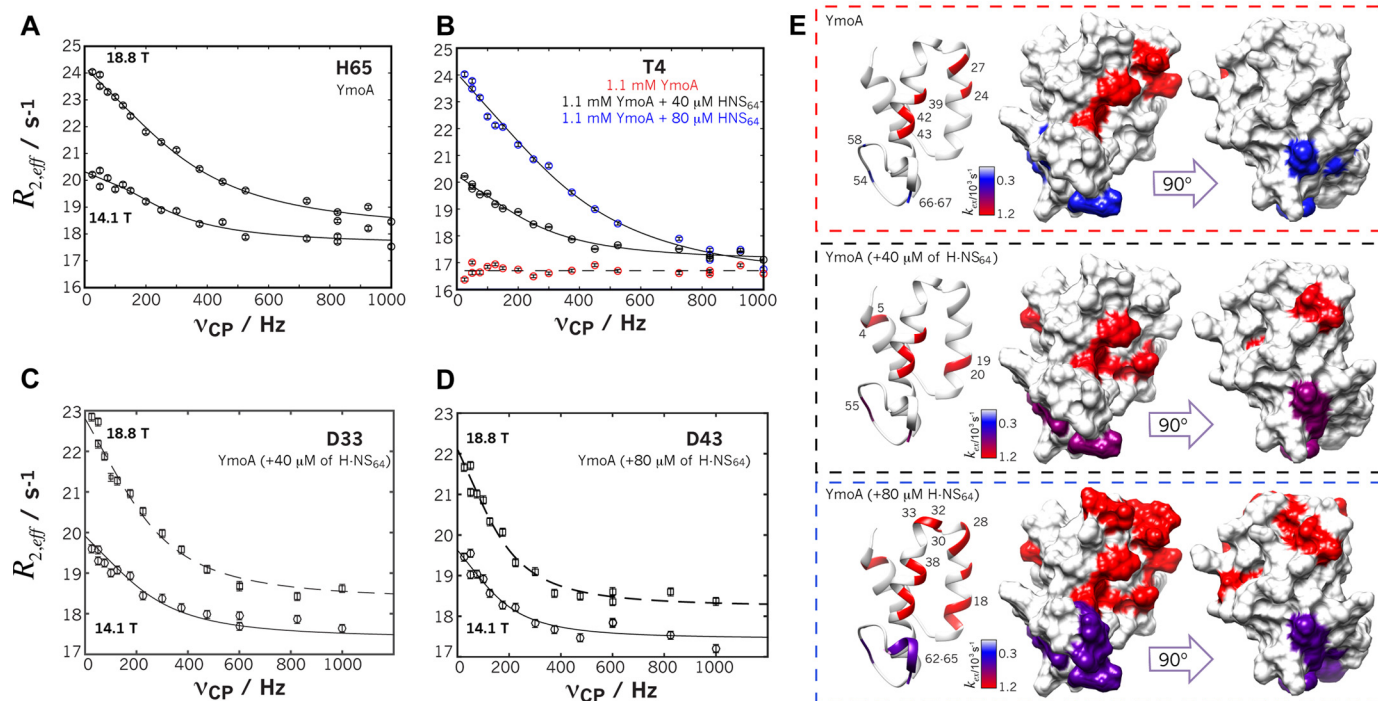
FIGURE 9. **CPMG dispersion profiles and mapping of affected residues.** *A*, H65 in helix 4 of free YmoA at two magnetic fields. *B*, residue T4 dynamics becomes observable only in the presence of H-NS$_{64}$. *C* and *D*, residues 33 and 43 of the core region in the presence of 40 μM and 80 μM of H-NS$_{64}$, respectively. The *solid lines* represent the simultaneously curve fitting to the data from the two magnetic fields. *B*, residues showing exchange are colored in the YmoA structure according to the exchange rates. The *three boxes* show the results in the absence (*red dashed box*) or presence of 40 μM (*black dashed-box*), 80 μM (*blue dashed-box*) of H-NS$_{64}$.

TABLE 3
CPMG kinetic parameters

YmoA	k_{ex}	p_B	k_+	k_-	[NaCl]
	s^{-1}	%	s^{-1}	s^{-1}	mM
Apo	1200 ± 130	2 ± 1	1177 ± 65	23 ± 8	200
Apo	500 ± 71	5 ± 3	493 ± 20	3 ± 2	100
Apo	152 ± 37	5 ± 2	142 ± 16	7 ± 5	50
+40 μM H-NS	1162 ± 104	5 ± 3	1104 ± 72	58 ± 15	200
+80 μM H-NS	1240 ± 116	6 ± 2	1162 ± 69	78 ± 10	200
D43N	0	0			200

FIGURE 10. **Ionic strength dependence of YmoA dynamics H-NS binding.** *A*, YmoA residues showing ms-μs exchange at different ionic strength. *B*, fluorescence anisotropy titrations of YmoA with H-NS$_{64}$ at various ionic strength values. The *inset* shows the linear dependence of K_D with ionic strength.

was reduced from 200 mM to 50 mM NaCl, the number of core residues showing collective motion increased from 5 to 16 residues. 11 of these residues belong to helices 2 and 3, and the short loop that connects them and 4 residues belong to helix 1. Thus, by reducing the ionic strength the collective motion was extended to embrace helix 1. The increased number of residues involved in the collective dynamics is expected to result in a reduction in the timescale of the motional process. Indeed, the exchange rate was progressively reduced nearly 2-fold and 8-fold when NaCl concentration was reduced to 100 and 50 mM, respectively.

Thus, electrostatic interactions are responsible for both the intrinsic dynamics of YmoA and the association to H-NS, stabilized through a charge zipper. This connection is strengthened by the observation that mutation of residue Asp-43 to asparagine completely abolished dynamics in the microsecond-millisecond time scale even in the presence of 80 μM H-NS$_{64}$. Residue Asp-43 plays a crucial role in the charge zipper, and mutation of the equivalent residue in Hha (Asp-48) completely abolished binding to H-NS (data not shown).

Discussion

Hha-like proteins modify the capacity of H-NS to silence specific DNA regions (8). H-NS binds and silences DNA

through the simultaneous interaction of the DNA binding domains from individual H-NS molecules assembled into linear oligomers. DNA selectivity, which in turn determines which genes are ultimately silenced, is achieved by indirect readout; DNA binding domains of H-NS sense local DNA distortions, and the formation of H-NS oligomers restricts the possible relative locations of adjacent DNA binding domains (49, 50). Hha binds to H-NS dimers formed by the interaction of N-terminal dimerization domain of two H-NS molecules. H-NS oligomerization involves a second dimerization site (residues 57–83) (44). A functional result of this interaction is that the Hha·H-NS complexes preferentially repress horizontally acquired genes.

The mechanism by which Hha binding induces changes in selectivity with respect to the genes that are repressed is not completely clear. Hha-like proteins and the NTD of H-NS contain an unusually large proportion of charged residues and a marked electrostatic asymmetry. The positive region of H-NS NTD has been suggested to interact with DNA according to the model of the DNA-H-NS complexes presented by Arold *et al.* (44) on the basis of the x-ray structure of the H-NS oligomers. According to this model, Hha-like molecules bind and mask the positively charged region of H-NS NTD. However, because of the electrostatic asymmetry of Hha itself, a new positively charged patch (from Hha) is displayed (19, 20), although at a different position with respect to the H-NS oligomer axis. The presence of Hha-like proteins is believed to change the "matching condition" between DNA binding and H-NS oligomerization and, therefore, the DNA silencing specificity (20, 21, 50). Mutagenesis in the positively charged region of Hha clearly demonstrates that this region is critical for transcriptional repression but not for H-NS binding (21, 24).

Binding of Hha to a strongly charged region of H-NS imposes the need for an electrostatic complex. However, electrostatic complexes are usually associated with a poor selectivity. In contrast, the tight network of multiple complementary interactions from three different proteins in the Hha complex with a H-NS dimer, conforming the observed charge zipper, ensures an exquisite selectivity (19, 20). A charge zipper combining intra- and intermolecular interactions stabilizing the translocation pore of TatA protein has been recently described (51).

Although electrostatic interactions play a clear role in intermolecular interactions (with H-NS or DNA), intramolecular electrostatic interactions may induce forces distorting the low energy packing of the helical core. The pervasive dynamics in the free form of YmoA may originate from the balance between electrostatically driven distortions and the hydrophobic interactions restoring forces. The fact that dynamics has been preserved by evolution suggests it may result in functional advantages.

Our results do not provide direct information on the possible conservation of the Hha/YmoA dynamics in the complexes, although the missing residues and structural variations between the two sites in the x-ray structure suggest that this may be the case. A direct functional correlation between dynamics and complex formation is supported by the changes observed in the number of residues involved in the microsecond-millisecond dynamics and the population of the minor conformation. This correlation is also supported by the effect of the D43N mutation of YmoA that completely abolished H-NS binding as well as μs-μs dynamics of the free form.

We can only speculate about how Hha/YmoA dynamics may influence function. We suggest at least three possible effects. (*a*) Due to its positively charged surface, a direct interaction between Hha and DNA was suggested (21). The existence of pervasive motions in the free molecule would increase the entropic penalty upon binding and may decrease spurious binding of Hha to DNA. (*b*) Hha binding to the NTD domain and the intrinsic dynamics of Hha-like proteins may change the flexibility of H-NS oligomers (52), thus modifying the selectivity. The fact that horizontally acquired DNA regions silenced by H-NS tend to be longer than those in the core genome (53) could make the flexibility of H-NS oligomers an important control element (50). (*c*) YmoA/Hha dynamics may facilitate binding to and/or dissociation of charge zipper complexes. Considering that electrostatic interactions are long range, the formation of the charge zipper may be compromised by local minima and dynamics may facilitate the optimization of the complex. Similarly, complete dissociation of an electrostatic complex may require large displacements of the charged elements before the interaction is effectively lost, and dynamics, if retained in the complex, may facilitate its dissociation. The similarity in the exchange rates observed in the presence and in the absence of H-NS would be compatible with a dynamic coupling between the intrinsic motions of Hha-like molecules and the formation or dissociation of the complex with H-NS.

References

1. WHO (2014) *Antimicrobial Resistance. Global Report on Surveillance*, World Health Organization Press
2. Ochman, H., Lawrence, J. G., and Groisman, E. A. (2000) Lateral gene transfer and the nature of bacterial innovation. *Nature* **405,** 299–304
3. Davies, J. (1994) Inactivation of antibiotics and the dissemination of resistance genes. *Science* **264,** 375–382
4. Davies, J., and Davies, D. (2010) Origins and evolution of antibiotic resistance. *Microbiol. Mol. Biol. Rev.* **74,** 417–433
5. Nieto, J. M., Carmona, M., Bolland, S., Jubete, Y., de la Cruz, F., and Juárez, A. (1991) The *hha* gene modulates haemolysin expression in *Escherichia coli. Mol. Microbiol.* **5,** 1285-1293
6. Cornelis, G. R., Sluiters, C., Delor, I., Geib, D., Kaniga, K., Lambert de Rouvroit, C., Sory, M. P., Vanooteghem, J. C., and Michiels T. (1991) *ymoA*, a *Yersinia enterocolitica* chromosomal gene modulating the expression of virulence functions. *Mol. Microbiol.* **5,** 1023–1034

7. Nieto, J. M., Madrid, C., Miquelay, E., Parra, J. L., Rodríguez, S., and Juárez, A. (2002) Evidence for direct protein-protein interaction between members of the enterobacterial Hha/YmoA and H-NS families of proteins. *J. Bacteriol.* **184,** 629–635

8. Baños, R. C., Vivero, A., Aznar, S., García, J., Pons, M., Madrid, C., and Juárez A. (2009) Differential regulation of horizontally acquired and core genome genes by the bacterial modulator H-NS. *PLoS Genet.* **5,** e1000513

9. Aznar, S., Paytubi, S., and Juárez, A. (2013) The Hha protein facilitates incorporation of horizontally acquired DNA in enteric bacteria. *Microbiology* **159,** 545–554

10. Madrid, C., García, J., Pons, M., and Juárez, A. (2007) Molecular evolution of the H-NS protein: interaction with Hha-like proteins is restricted to *Enterobacteriaceae. J. Bacteriol.* **189,** 265–268

11. Takeda, T., Yun, C.-S., Shintani, M., Yamane, H., and Nojiri, H. (2011) Distribution of genes encoding nucleoid-associated protein homologs in plasmids. *Int. J. Evol. Biol.* **2011,** 685015

12. García-Contreras, R., Zhang, X. S., Kim, Y., and Wood, T. K. (2008) Protein translation and cell death: the role of rare tRNAs in biofilm formation and in activating dormant phage killer genes. *PLoS ONE* **3,** e2394

13. Hong, S. H., Lee, J., and Wood, T. K. (2010) Engineering global regulator Hha of *Escherichia coli* to control biofilm dispersal. *Microb. Biotechnol.* **3,** 717–728

14. Sharma, V. K., and Bearson, B. L. (2013) Hha Controls *Escherichia coli* O157:H7 biofilm formation by differential regulation of global transcriptional regulators FlhDC and CsgD. *Appl. Environ. Microbiol.* **79,** 2384–2396

15. Mikulskis, A. V., and Cornelis, G. R. (1994) A new class of proteins regulating gene expression in enterobacteria. *Mol. Microbiol.* **11,** 77–86

16. Balsalobre, C., Juárez, A., Madrid, C., Mouriño, M., Prenafeta, A., and Muñoa, F. J. (1996) Complementation of the hha mutation in *Escherichia coli* by the ymoA gene from *Yersinia enterocolitica*: dependence on the gene dosage. *Microbiology* **142,** 1841–1846

17. Yee, A., Chang, X., Pineda-Lucena, A., Wu, B., Semesi, A., Le, B., Ramelot, T., Lee, G. M., Bhattacharyya, S., Gutierrez, P., Denisov, A., Lee, C. H., Cort, J. R., Kozlov, G., Liao, J., Finak, G., Chen, L., Wishart, D., Lee, W., McIntosh, L. P., Gehring, K., Kennedy, M. A., Edwards, A. M., and Arrowsmith, C. H. (2002) An NMR approach to structural proteomics. *Proc. Natl. Acad. Sci. U.S.A.* **99,** 1825–1830

18. McFeeters, R. L., Altieri, A. S., Cherry, S., Tropea, J. E., Waugh, D. S., and Byrd R. A. (2007) The high-precision solution structure of *Yersinia* modulating protein YmoA provides insight into interaction with H-NS. *Biochemistry* **46,** 13975–13982

19. García, J., Madrid, C., Juárez, A., and Pons, M. (2006) New roles for key residues in helices H1 and H2 of the *Escherichia coli* H-NS N-terminal domain: H-NS dimer stabilization and Hha binding. *J. Mol. Biol.* **359,** 679–689

20. de Alba, C. F., Solórzano, C., Paytubi, S., Madrid, C., Juarez, A., García, J., and Pons, M. (2011) Essential residues in the H-NS binding site of Hha, a co-regulator of horizontally acquired genes in Enterobacteria. *FEBS Lett.* **585,** 1765–1770

21. Ali, S. S., Whitney, J. C., Stevenson, J., Robinson, H., Howell, P. L., and Navarre, W. W. (2013) Structural Insights into the Regulation of Foreign Genes in *Salmonella* by the Hha/H-NS Complex. *J. Biol. Chem.* **288,** 13356–13369

22. Paytubi, S., García, J., and Juárez, A. (2011) Bacterial Hha-like proteins facilitate incorporation of horizontally transferred DNA. *Open Life Sciences* **6,** 879–886

23. García, J., Cordeiro, T. N., Nieto, J. M., Pons, I., Juárez, A., and Pons, M. (2005) Interaction between the bacterial nucleoid associated proteins Hha and H-NS involves a conformational change of Hha. *Biochem. J.* **388,** 755–762

24. Cordeiro, T. N., Garcia, J., Pons, J. I., Aznar, S., Juárez, A., and Pons, M. (2008) A single residue mutation in Hha preserving structure and binding to H-NS results in loss of H-NS mediated gene repression properties. *FEBS Lett.* **582,** 3139–3144

25. Battiste, J. L., and Wagner, G. (2000) Utilization of site-directed spin labeling and high-resolution heteronuclear nuclear magnetic resonance for global fold determination of large proteins with limited nuclear Over-hauser effect data. *Biochemistry* **39,** 5355–5365

26. Dominguez, C., Boelens, R., and Bonvin, A. M. (2003) HADDOCK: a protein-protein docking aproach based on biochemical or biophysical information. *J. Am. Chem. Soc.* **125,** 1731–1737

27. Emekli, U., Schneidman-Duhovny, D., Wolfson, H. J., Nussinov, R., and Haliloglu, T. (2008) HingeProt: automated prediction of hinges in protein structures. *Proteins* **70,** 1219–1227

28. de Vries, S. J., van Dijk, A. D., Krzeminski, M., van Dijk, M., Thureau, A., Hsu, V., Wassenaar, T., and Bonvin, A. M. (2007) HADDOCK versus HADDOCK: new features and performance of HADDOCK2.0 on the CAPRI targets. *Proteins* **69,** 726–733

29. Iwahara, J., Schwieters, C. D., and Clore, G. M. (2004) Ensemble approach for NMR structure refinement against ^{1}H paramagnetic relaxation enhancement data arising from a flexible paramagnetic group attached to a macromolecule. *J. Am. Chem. Soc.* **126,** 5879–5896

30. García de la Torre, J., Huertas, M. L., and Carrasco, B. (2000) HYDRONMR: prediction of NMR relaxation of globular proteins from atomic-level structures and hydrodynamic calculations. *J. Magn. Reson.* **147,** 138–146

31. Tollinger, M., Skrynnikov, N. R., Mulder, F. A., Forman-Kay, J. D., and Kay, L. E. (2001) Slow dynamics in folded and unfolded states of an SH3 domain. *J. Am. Chem. Soc.* **123,** 11341–11352

32. Loria, J. P., Rance, M., and Palmer, A. G. (1999) A TROSY CPMG sequence for characterizing chemical exchange in large proteins. *J. Biomol. NMR* **15,** 151–155

33. Mulder, F. A., Skrynnikov, N. R., Hon, B., Dahlquist, F. W., and Kay, L. E. (2001) Measurement of slow (micros-μs) time scale dynamics in protein side chains by ^{15}N relaxation dispersion NMR spectroscopy: application to Asn and Gln residues in a cavity mutant of T4 lysozyme. *J. Am. Chem. Soc.* **123,** 967–975

34. Carver, J. P., and Richards, R. E. (1972) A general two-site solution for the chemical exchange produced dependence of T_2 upon the Carr-Purcell pulse separation. *J. Magn. Reson.* **6,** 89–105

35. Gabdoulline, R. R., Stein, M., and Wade, R. C. (2007) qPIPSA: relaing enzymatic kinetic parameters and interaction fields. *BMC Bioinformatics* **8,** 373

36. Richter, S., Wenzel, A., Stein, M., Gabdoulline, R. R., and Wade, R. C. (2008) webPIPSA: a web server for the comparison of protein interaction properties. *Nucleic Acids Res.* **36,** W276–W280

37. Biasini, M., Bienert, S., Waterhouse, A., Arnold, K., Studer, G., Schmidt, T., Kiefer, F., Cassarino, T. G., Bertoni, M., Bordoli, L., and Schwede, T. (2014) SWISS-MODEL: modeling protein tertiary and quaternary structure using evolutionary information. *Nucleic Acids Res.* **42,** W252–W258

38. UniProt Consortium (2014) Activities at the Universal Protein Resource. *Nucleic Acids Res.* **42,** D191–D198

39. Rocchia, W., Sridharan, S., Nicholls, A., Alexov, E., Chiabrera, A., and Honig, B. (2002) Rapid grid-based construction of the molecular surface and the use of induced surface charge to calculate reaction field energies: applications to the molecular systems and geometric objects. *J. Comput. Chem.* **23,** 128–137

40. Kieslich, C. A., and Morikis, D. (2012) The two sides of complement C3d: evolution of electrostatics in a link between innate and adaptive immunity. *PLoS Comput. Biol.* **8,** e1002840

41. Pettersen, E. F., Goddard, T. D., Huang, C. C., Couch, G. S., Greenblatt, D. M., Meng, E. C., and Ferrin, T. E. (2004) USCF Chimera: a visualization system for exploratory research and analysis. *J. Comput. Chem.* **25,** 1605–1612

42. Konarev, P. V., Volkov, V. V., Sokolova, A. V., Koch, M. H. J., and Svergun, D. I. (2003) PRIMUS: a Windows PC-based system for small-angle scattering data analysis. *J. Appl. Cryst.* **36,** 1277–1282

43. Svergun, D. I., Barberato, C., and Koch, M. H. J. (1995) CRYSOL: a program to evaluate x-ray solution scattering of biological macromolecules from atomic coordinates. *J. Appl. Cryst.* **28,** 768–773

44. Arold, S. T., Leonard, P. G., Parkinson, G. N., and Ladbury, J. E. (2010) H-NS forms a superhelical protein scaffold for DNA condensation. *Proc. Natl. Acad. Sci. U.S.A.* **107,** 15728–15732

45. García, J., Madrid, C., Cendra, M., Juárez, A., and Pons, M. (2009) N9L and L9N mutations toggle Hha binding and hemolysin regulation by *Esche-*

richia coli and *Vibrio cholerae* H-NS. *FEBS Lett.* **583,** 2911–2916

46. Clore, G. M., and Iwahara, J. (2009) Theory, practice, and applications of paramagnetic relaxation enhancement for the characterization of transient low-population states of biological macromolecules and their complexes. *Chem. Rev.* **109,** 4108–4139

47. Bloch, V., Yang, Y., Margeat, E., Chavanieu, A., Augé, M. T., Robert, B., Arold, S., Rimsky, S., and Kochoyan, M. (2003) The H-NS dimerization domain defines a new fold contributing to DNA recognition. *Nat. Struct. Biol.* **10,** 212–218

48. Zhou, H. X. (2001) Disparate ionic-strength dependencies of on and off rates in protein-protein association. *Biopolymers* **59,** 427–433

49. Cordeiro, T. N., Schmidt, H., Madrid, C., Juárez, A., Bernadó, P., Griesinger, C., García, J., and Pons, M. (2011) Indirect DNA readout by an H-NS related protein: structure of the DNA complex of the C-terminal domain of Ler. *PLoS Pathog.* **7,** e1002380

50. Fernández-de-Alba, C., Berrow, N. S., Garcia-Castellanos, R., García, J., and Pons, M. (2013) On the origin of the selectivity of plasmidic H-NS towards horizontally acquired DNA: linking H-NS oligomerization and cooperative DNA binding. *J. Mol. Biol.* **425,** 2347–2358

51. Walther, T. H., Gottselig, C., Grage, S. L., Wolf, M., Vargiu, A. V., Klein, M. J., Vollmer, S., Prock, S., Hartmann, M., Afonin, S., Stockwald, E., Heinzmann, H., Nolandt, O. V., Wenzel, W., Ruggerone, P., and Ulrich, A. S. (2013) Folding and self-assembly of the TatA translocation pore based on a charge zipper mechanism. *Cell* **152,** 316–326

52. Renault, M., García, J., Cordeiro, T. N., Baldus, M., and Pons, M. (2013) Protein oligomers studied by solid-state NMR: the case of the full-length nucleoid-associated protein histone-like nucleoid structuring protein. *FEBS J.* **280,** 2916–2928

53. Kahramanoglou, C., Seshasayee, A. S., Prieto, A. I., Ibberson, D., Schmidt, S., Zimmermann, J., Benes, V., Fraser, G. M., and Luscombe, N. M. (2011) Direct and indirect effects of H-NS and Fis on global gene expression control in *Escherichia coli*. *Nucleic Acids Res.* **39,** 2073–2091

A Three-protein Charge Zipper Stabilizes a Complex Modulating Bacterial Gene Silencing

Tiago N. Cordeiro, Jesús García, Pau Bernadó, Oscar Millet and Miquel Pons

Access the most updated version of this article at doi: 10.1074/jbc.M114.630400

Find articles, minireviews, Reflections and Classics on similar topics on the JBC Affinity Sites.

Alerts:

- When this article is cited
- When a correction for this article is posted

Click here to choose from all of JBC's e-mail alerts

This article cites 52 references, 15 of which can be accessed free at
http://www.jbc.org/content/290/35/21200.full.html#ref-list-1